Lab on a Chip

PAPER

View Article Online
View Journal | View Issue

Cite this: *Lab Chip*, 2019, **19**, 4043

Blood platelet enrichment in mass-producible surface acoustic wave (SAW) driven microfluidic chips†

Cynthia Richard,[a] Armaghan Fakhfouri,[a] Melanie Colditz,[a] Friedrich Striggow,[a] Romy Kronstein-Wiedemann,[b] Torsten Tonn,[b] Mariana Medina-Sánchez,[a] Oliver G. Schmidt,[a] Thomas Gemming[a] and Andreas Winkler *[a]

The ability to separate specific biological components from cell suspensions is indispensable for liquid biopsies, and for personalized diagnostics and therapy. This paper describes an advanced surface acoustic wave (SAW) based device designed for the enrichment of platelets (PLTs) from a dispersion of PLTs and red blood cells (RBCs) at whole blood concentrations, opening new possibilities for diverse applications involving cell manipulation with high throughput. The device is made of patterned SU-8 photoresist that is lithographically defined on the wafer scale with a new proposed methodology. The blood cells are initially focused and subsequently separated by an acoustic radiation force (ARF) applied through standing SAWs (SSAWs). By means of flow cytometric analysis, the PLT concentration factor was found to be 7.7, and it was proven that the PLTs maintain their initial state. A substantially higher cell throughput and considerably lower applied powers than comparable devices from literature were achieved. In addition, fully coupled 3D numerical simulations based on SAW wave field measurements were carried out to anticipate the coupling of the wave field into the fluid, and to obtain the resulting pressure field. A comparison to the acoustically simpler case of PDMS channel walls is given. The simulated results show an ideal match to the experimental observations and offer the first insights into the acoustic behavior of SU-8 as channel wall material. The proposed device is compatible with current (Lab-on-a-Chip) microfabrication techniques allowing for mass-scale, reproducible chip manufacturing which is crucial to push the technology from lab-based to real-world applications.

Received 13th August 2019,
Accepted 21st October 2019

DOI: 10.1039/c9lc00804g

rsc.li/loc

The capacity to precisely separate and manipulate suspended particles, cells or other biological matter, is a critical process in many applications of biology and medicine for disease diagnosis, genetic analysis, drug screening and therapeutics.[1–4] Since blood samples are one of the most important sources of information regarding the health status of a patient, the improvement of current blood based diagnostic and analysis methods is crucial.

Existing diagnostic technologies for blood samples employ cell counting (Coulter principle),[5] erythrocyte sedimentation (ESR),[6] enzyme-linked immunosorbent assay (ELISA),[7] polymerase chain reaction (PCR)[8] and mass spectrometry (MS).[9] These methods rely on accurate sample purification and pre-treatment, are time consuming and labor intensive, and are restricted to laboratory use which can be rather costly.[10] Furthermore, many of these technologies are not sufficiently sensitive for low biomarker concentrations. Thus, more robust, sensitive and rapid technologies are required for blood cell separation, plasma extraction and diagnostics. Current acoustofluidic technologies, such as SAW-based actuators, have been gaining a lot of interest in medical technology owing to their biocompatibility,[11] their straightforward implementation in other chip-based microfluidic techniques, and their ability to manipulate cells in a label-free and contactless manner.[12–14] In addition, such devices are attractive for rapid point-of-care testing since whole blood can be directly used without the need for any pre-treatment steps.[15] Acoustofluidic devices have already been used in a variety of particle and cell manipulation applications such as focusing,[16,17] patterning,[18–20] separation,[21,22] and particularly for RBCs and PLTs separation.[23] However, typical SAW-based devices demonstrated in lab environments employ microchannels fabricated *via* cast-molding of polydimethylsiloxane (PDMS), a tedious and rather inefficient fabrication process. PDMS

[a] *Leibniz-IFW Dresden, Helmholtzstr. 20, 01069 Dresden, Germany. E-mail: a.winkler@ifw-dresden.de*
[b] *Experimentelle Transfusionsmedizin, Medizinische Fakultät Carl Gustav Carus der Technischen Universität Dresden/DRK-Blutspendedienst Nord-Ost gGmbH, Blasewitzer str. 68/70, 01370 Dresden, Germany*

† Electronic supplementary information (ESI) available. See DOI: 10.1039/c9lc00804g

remains difficult and expensive to integrate in commercially produced microfluidic devices owing to long curing times, bonding inconsistencies, and alignment issues. Moreover, there is a potentially undesirable gas and solvent permeability and absorption/adsorption inherent to this silicone polymer as well as a low chemical and mechanical stability.

In order to proceed from lab-based to real-world applications, reproducible, accurate and more efficient methods for on-chip microchannel structuring are required. There is therefore a trend in the more general field of microfluidics to move towards materials that can be used to lithographically define channels directly on top of the active microfluidic chips, such as photoresists. One of the most commonly used, and best characterized photoresists for microtechnology is the epoxy-based, negative spin-on resist, SU-8.[24] It offers significant potential for microfluidic systems where the channel elements can be reliably positioned with chip-wide, micron-scale accuracy, eliminating the need for substrate bonding. Due to its straight forward microfabrication process, which is congruent to mass-scale manufacturing in the micro-electronics industry,[25] it enables easy on-chip integration and is therefore a favorable alternative to PDMS in acoustofluidic applications. On the other hand, the acoustic behavior of PDMS is well characterized and its specific acoustic impedance (1.04 MPa s m^{-1}),[26] below that of water (1.48 MPa s m^{-1} at 25 °C),[26] minimizes interfering resonances due to reduced acoustic reflections. Although a change in channel wall material would be beneficial regarding technological needs, typical polymers, glasses and metals have a higher acoustic impedance (*e.g.* impedance of SU-8 is 3.59 MPa s m^{-1}) than that of water, resulting in a more complex acoustic behavior due to increased reflections at the fluid–solid interface.[26,27] Thus, the channel walls and the properties of the wall material must be taken into consideration when planning the geometry of the channel layout, and for the task specific design of the SAW-chip.

To date, few publications mention SU-8 microchannels in combination with SAW.[28–32] From these, only Mu *et al.*[30] used an approach similar to the one shown here. They created SU-8 microfluidic channels with large wall widths, for SAW-based particle concentration where PDMS was used as a cover with in- and outlet openings only. The authors demonstrated a narrowing of the particle stream in their SU-8 device in comparison to results previously reported, but no cell sorting was demonstrated. In our work, an analogous device is further optimized to be more power efficient and to produce less parasitic heat by viscous attenuation of SAWs in comparison to the device introduced by Mu *et al.* The more complex task of cell focusing and separating was successfully accomplished for the first time in such a setup. Also, optical lithography was used to create thin, open microfluidic channels out of SU-8 directly onto 4″ wafers. A PDMS cover was used to seal the SU-8 microchannel resulting in an exceptional platform for acoustic enrichment of PLTs with a higher separation efficiency, substantially higher cell throughput and significantly lower applied powers to current state-of-the-art. The separated platelets and red blood cells were collected at different outlets to perform platelet activation test and flow cytometry. Furthermore, a comprehensive analysis of the wave field generated on the chip surface and inside the microfluidic channel was performed. Using a fully coupled finite element method (FEM) simulation, for the first time, we demonstrate the influence of SU-8 side walls on the acoustic wave field within the fluid-filled microchannel, with excellent agreement to the experimental observations.

Results

Device operation

The SAW-based device employs standing surface acoustic wave (SSAW) fields inside a fluidic microchannel. The SSAW fields are developed by the superposition of counter-propagating traveling surface acoustic waves (TSAWs) emanating from two sets of opposing interdigital transducers (IDTs); Fig. 1 and 2(a) depict the schematic working principle of the two-stage device. When the TSAWs arrive at the solid/fluid (lithium niobate ($LiNbO_3$)/water) interface, most of the traveling waves are refracted into the fluid as longitudinal waves at the Rayleigh angle $\theta(\sin(\theta) = C_f/C_m$, where C_f and C_m are the wave velocities of fluid and solid respectively), while the SAW is attenuated on the surface of the substrate (leaky SAW).

The interference of the opposing incident longitudinal waves subsequently forms a standing wave field inside the fluid-filled channel. Amplitude distributions of the resultant pressure field in the channel, however, are strongly affected by several features. Firstly, the longitudinal waves are reflected at the liquid/SU-8 interface due to the large difference in the acoustic impedance of SU-8 and water. Secondly, in contrast to PDMS, SU-8 has a higher acoustic impedance and a lower acoustic absorption. As follows, longitudinal waves are likely excited within the SU-8 walls, caused by acoustic refraction at the $LiNbO_3$/SU-8 interface, leading to additional longitudinal waves radiating from the channel walls into the fluid (Fig. 2(a), inset).

The presence of a cell within this pressure field, in the fluid domain, gives rise to the acoustic radiation force (ARF), leading to the migration of cells towards certain pressure regions.[33–36] The acoustic contrast factor, ϕ, a function of density and compressibility of the medium and of the cell, indicates whether the cell will be attracted to a pressure node ($+\phi$) or to a pressure anti-node ($-\phi$).[37] Since the value of ϕ for RBCs and PLTs in a phosphate-buffered saline (PBS) solution (ρ = 1004 kg m^{-3}, c = 1508.2 m s^{-1}, $\beta = 1/\rho c^2$)[38] was calculated to be 0.35 and 0.21,[15] respectively, these cells will be trapped in pressure nodes. Furthermore, a cell exposed to the SSAW field in this system is also subjected to a viscous drag force induced by the fluid flow. Size-based cell separation is possible considering that the ARF and the drag force are

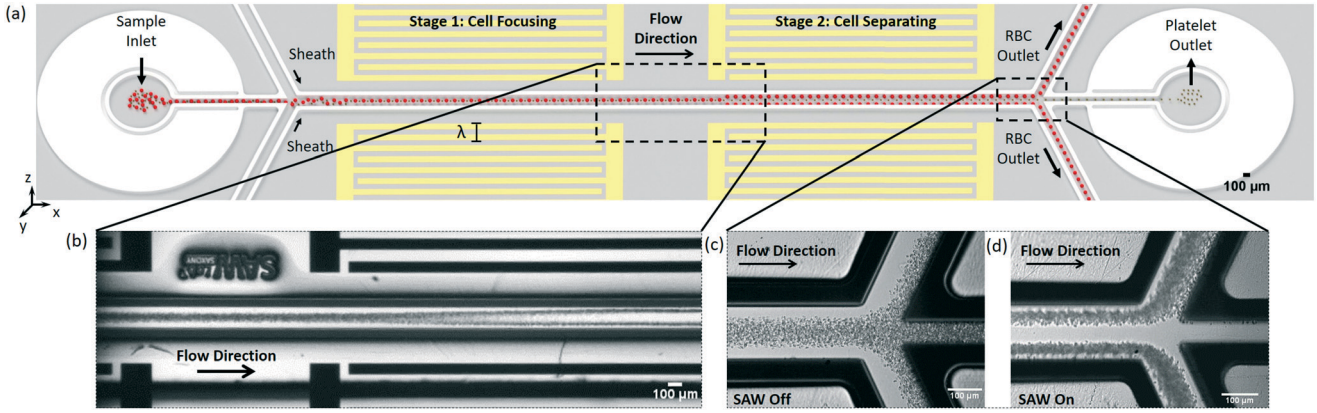

Fig. 1 Schematic illustration and images of the SAW-based device for cell separation. (a) Illustration of the chip layout for cell focusing, using the first pair of interdigital transducers (IDTs), followed by separation at the second set of IDTs, inside of the SU-8 microchannel. The IDTs and the SU-8 channel walls, were fabricated *via* lithography directly onto a $LiNbO_3$ wafer. (b) An overview of the results showing the SSAW focusing and separation of the RBCs and PLTs. (c) Results obtained with the RBCs and PLTs flowing in all three outlets with no applied SAW. (d) The separation obtained at the outlets when 150 mW of power was applied to the first pair of IDTs for cell focusing and 120 mW was applied to the second pair of IDTs for separating.

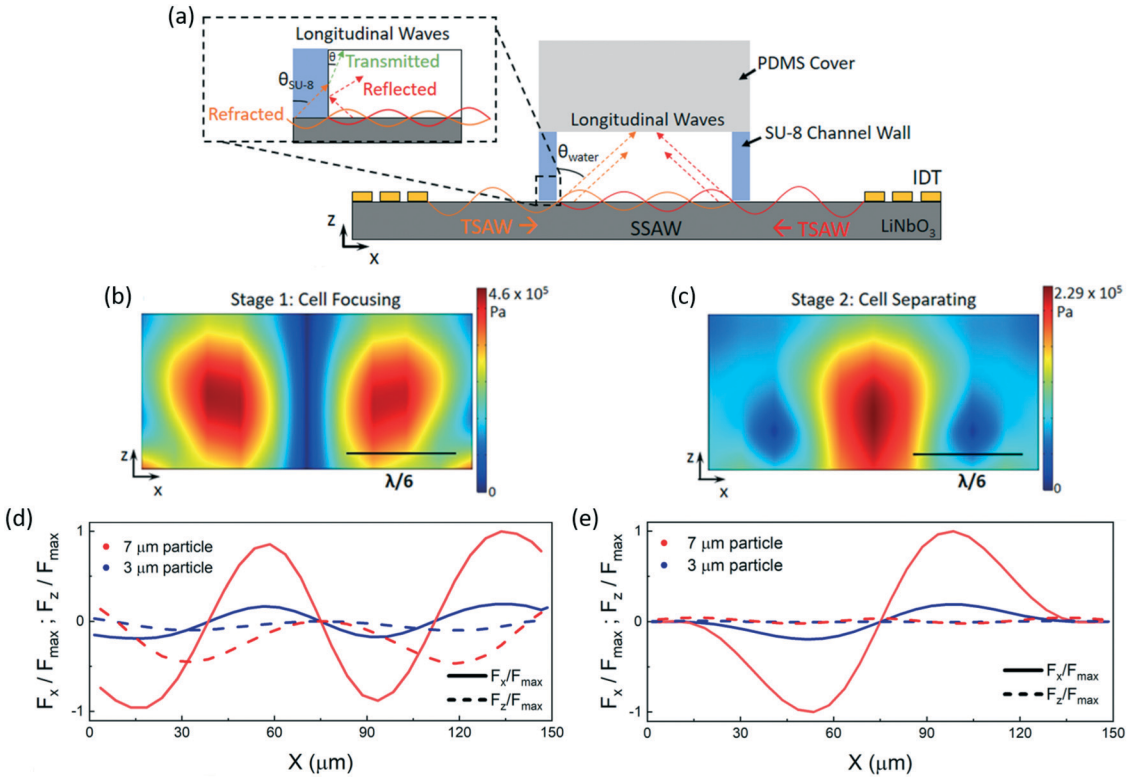

Fig. 2 Acoustic behavior of SU-8 as the channel wall material. COMSOL Multiphysics simulation showing the pressure node system created inside of the microfluidic channel at the desired resonant frequency. (a) Cross-sectional representation of the device where a PDMS cover is used to seal the SU-8 channel walls. A pair of opposing IDTs excite TSAWs that establish a SSAW inside of the microfluidic channel. The arrows represent the refracted waves which radiate into the liquid at the Rayleigh angle θ. Cells flowing through the channel feel a different acoustic force in the SSAW region and are therefore attracted to different pressure nodes based on their size. Inset demonstrating the refraction and transmission of longitudinal waves at the substrate/SU-8 and the SU-8/fluid interface, respectively. In addition, reflections at the fluid/SU-8 interface from the longitudinal wave from the opposing IDT also affect the wave field generated in the channel. Note: for every incident wave there is a reflected and transmitted component (some not shown in diagram). FEM simulations indicating the time averaged absolute pressure field ($<|p|>$) for the focusing stage of the device (b) and for the separation stage (c). (d) and (e) demonstrate the normalized spatial radiation forces acting on particles of similar sizes to the blood cells in the focusing stage, and separation stage, respectively, where the *x*-axis represents the displacement and the *y*-axis represents the force amplitude.

proportional to the cell radius (FARF $\sim R^3$, $F_{Drag} \sim R$, where R is the cell radius).[39] As such, the cell response is dictated by the dominance of these two forces (ARF and dragforce) and larger cells, for instance RBCs, will be more affected by the ARF and thus will move towards pressure nodes faster than smaller cells.

The first stage of the device (Fig. 1(a)) focuses all cells into a central pressure node, whereas separation takes place at the second stage. Here, larger cells (RBCs) will experience a larger radiation force and will therefore move towards pressure-nodes created near the channel walls faster than smaller cells (PLTs), which will remain in the center of the channel and continue along the flow.

Blood cell separation

Prior to experimentation with cells at whole blood concentrations, the device was tested with polystyrene particles with radii comparable to blood cell components (7 μm, representative of RBCs and 3 μm, representative of PLTs). Once the device functionality was verified, a diluted sample of RBCs and PLTs was tested to optimize the flow rates, and the applied powers.

The microfluidic channel consists of three inlets and three outlets on both ends of a larger central channel (see Fig. S1† for the overview of the chip layout). The blood sample is injected through the central inlet and a two-sided sheath flow is applied *via* the adjacent channels (Fig. 1(a)). The sheath flow ensures that the cells are initially located in the central channel region and experience an acoustic radiation force only towards the center nodal-region. The flow rates of the blood sample mixture and of the sheath flow were all set to 0.5 μL min^{-1}, resulting in a total flow rate of 1.5 μL min^{-1} (2.7×10^6 cells per min) in the main channel. Fig. 1(c) shows the blood sample flowing through all three of the outlets when no SAW is applied. For optimal cell separation, a power of 150 mW at a driving frequency of 13 MHz was applied to the first pair of IDTs for cell focusing, and a power of 120 mW at a driving frequency of 12.7 MHz was applied to the second pair of IDTs for cell separation. In the second stage, it can be seen that the RBCs become trapped in pressure nodes created near the channel walls and are thus directed towards the upper and lower outlets. The PLTs remain in the central region and exit through the central outlet (Fig. 1(d), see also Movies S1 to S4†).

Flow cytometric analysis was performed on the collected samples and the purity of cells at each individual outlet was measured through platelet labelling. The separation efficiency, given as the ratio of the target cell purity at the desired outlet to the total number of target cells collected at all outlets, was found to be 86% for the PLTs and 77% for the RBCs. In addition, the concentration factor was calculated as the ratio of purity of desired cells at the desired outlet to the total number of these cells found in the original sample solution. It was found that the PLTs were concentrated at the middle outlet with a factor of 7.7 (an increase from 5.5% cell concentration in the original sample solution to 42.9% in the collected sample). Further optimization of the outlet channel geometry based on the current setup is expected to lead to an increase in separation efficiency and purity of the separated samples. The optimization may especially include the change of channel width ratio between outer and central channels (to adjust pressure loss), as well as the angle of the outer channels (to reduce shear forces at the trifurcation point). In addition, due to the high concentration of RBCs used in the experiment, an overflow effect was observed due to a lack of space in the central outlet. Increasing the cross-sectional area of the center outlet would thus eliminate the overflowing of RBCs into the neighbouring outlets and increase the separation efficiency of the device. To verify that little to no shear-induced stress was applied by the SSAW to the cells, the PLT activation was measured through the use of the antibody CD62P-PE (BD Bio-sciences, USA). An activation comparable to fresh blood samples was observed; deformation and coagulation of the cells did not occur. Considering that RBCs are much less sensitive to shear-stress than PLTs, they are expected to remain unaffected.

Characterization and numerical simulation

A high frequency laser-Doppler vibrometer (LDV) was used to measure the amplitude of the standing wave fields excited on the chip surface (Fig. S2†). To probe the physics of the two-staged separation, fully-coupled 3D numerical simulations of the SSAW field in the time-domain were obtained using the exact geometries and parameters used for the chip layout, whereby the SSAW amplitude was scaled according to the vibrometer data. From these simulations, the time-averaged absolute pressure fields, $<|p|>$, were calculated and can be seen in Fig. 2(b and c). The simulations indicate the developed longitudinal pressure nodes (in blue) and the surrounding two-dimensional pressure field in a channel cross-section. The results reveal a pressure node in the center of the channel for the focusing stage of the device, where a 180° phase shift (due to the electrode configuration) is present between the IDTs (Fig. 2(b), see also Movie S5†). Since low pressure regions can be seen extending to the channel walls, particles are also expected to accumulate there. This parasitic effect can be overcome by applying a sheath flow forcing the cells to collect in the central node. Experiments regarding the necessity of the sheath flow were conducted and the results can be seen in Fig. S3.† It is important to note that hydrodynamic focusing is simply used to keep the cells in the desired node and that SAW focusing is essential for narrowing the cell stream and for aligning the stream in the center of the fluidic channel. In addition, the SAW focusing provides the cells with a low-shear environment (shear stress is at a minimum at the center of the flow profile).

Furthermore, FEM simulations demonstrating the spatial variation in the acoustic radiation forces (x and z

components both normalized by the maximum force) experienced by particles (here used as a substitution for the cells) placed in a sound pressure field were also conducted for both stages of the device (Fig. 2(d) and (e)). The forces are determined by moving the particles to various locations across a defined line of interest that cuts through the pressure nodes and anti-nodes along the channel width, with a step size of 5 μm ($\lambda_{SAW}/60$). At the focusing stage, there is a stable trapping location at x = 75 μm ($\lambda_{SAW}/4$) where the x and z components of the force are zero for both particle sizes of 3 μm and 7 μm. As a result, both particle sizes are trapped in this location; focusing occurs. At the separation stage, the larger particles experience a higher force amplitude (x-component), compared to the smaller particles, at the central region and will migrate to the neighboring pressure nodes near the channel walls. Here, the applied power is adjusted to allow for migration of larger particles (akin to RBCs) whilst preventing migration of smaller particles (akin to PLTs) to the side walls.

At the second stage, where no phase shift is present between the two TSAWs, two pressure nodes are established near the channel walls (Fig. 2(c), see also Movie S5†). From the simulations, the extent of the pressure node regions, as well as the spacing between them, were measured and compared to those of the separated blood streams obtained experimentally (Fig. S5†). The accordance of the obtained results verify the accuracy of the predictions made through the simulations. At the first stage however, the width of the focused blood stream measured experimentally extends slightly into the higher pressure region in contrast to the numerical simulation. This is assumed to be caused by a high concentration of RBCs.

For comparison, a simulation with PDMS as the channel wall material was also completed (Fig. S4†) to demonstrate the strong effects that the SU-8 properties have on the wave field. It was found that the Rayleigh angle of PDMS is 15.6° whereas that of SU-8 is 50°. This means that in the case of SU-8 the incident SAW which radiates a longitudinal pressure wave in the outer SU-8 wall will be refracted, and will be transmitted into the fluid at the SU-8/fluid interface (Fig. 2(a), inset). The effects of the additional transmitted and reflected waves in the case of SU-8 is easily visible when comparing the wave field in the $LiNbO_3$ substrate and in the fluid filled channel. In most studies published, the walls are conventionally neglected for the case of PDMS, however, for SU-8 this cannot be done due its more complex acoustic behaviour. As such, the lateral and vertical position of the pressure nodes is dependent on the acoustic boundary condition.

Discussion

In this work, a SAW-based, lithographically fabricated microfluidic chip for PLT enrichment, at a concentration typically found in whole blood, is presented alongside a comprehensive experimental and numerical study of the electric and acoustic behavior of the device, and the wave field inside of the fluid-filled microchannel. In contrast to conventionally used PDMS-based microchannels, all geometrically-critical microchannel features are defined with lithographic resolution, while the silicone cover lid can be produced in a more simple way, *e.g.* by stencil techniques. The wafer-scale microfabrication technique used is reliable, precise, highly reproducible, compatible with current Lab-on-a-Chip techniques, enabling for the first time, the mass-production of chips.

For the application demonstrated here, PDMS is a suitable cover material. However, if an application requires a more chemically stable cover layer, or if gas and solvent permeability has to be reduced, either a change of cover layer material towards a more chemically stable, flexible polymer, *e.g.* perfluor-natural rubber (FFKM/FFPM), or a chemically-compatible coating of the inner channel wall (*e.g. via* synthesis of SiO_2 from solution), may be possible and compatible with the presented approach.

The chips have a simple interface to the signal and fluid peripheral sources, allowing for their future integration onto point-of-care devices. Moreover, they can be used as consumables, which is an important feature, *e.g.* to avoid cross-contamination of analyzed blood samples. The fully-coupled 3D simulations considering the absolute pressure field in the fluidic microchannel offer insight into the acoustic phenomena that gives rise to cell manipulation. Furthermore, they highlight the significant influence the different material properties of SU-8 in comparison to PDMS as the channel wall material, have on the acoustic behavior of the proposed technology.

The excellent material properties of SU-8 combined with thin channel wall widths, and refined IDT layouts with lower losses, allow for effective SAW excitation with low applied powers. For instance, Jo *et al.* employed powers up to, and sometimes exceeding, 1 W, in a PDMS device for the separation of particles with similar sizes to blood cells (with flow rates from 1 μL min^{-1} to 8 μL min^{-1}, however with undetermined separation efficiencies).[40] In their SU-8 channel, Mu *et al.* used flow rates of 4 μL min^{-1}, and 4 μL min^{-1} to 12 μL min^{-1} for the blood sample and sheath flows, respectively, with a driving power of 3 W for particle concentrating.[30] A high power was required in their device due to very wide channel walls, in comparison to the approach reported here where a maximum of 150 mW was needed. They reported the isolation of exosomes from an extracellular vesicle mixture with a purity of 98.4%, and a blood cell removal rate of 99.999%. The SAW-based separation of particles, or cells, with power levels comparable to the device presented here has not yet been reported in literature. Furthermore, a lower sheath flow rate, which leads to a less diluted sample, and therefore to a higher cell throughput is reported here. For instance in their device, Nam *et al.*, separated white blood cells (WBCs) and RBCs from PLTs in a PDMS device with a separation efficiency of 99.9% and 74.1%, respectively, but with highly diluted samples (5 μL min^{-1} of sheath flow and 0.25 μL min^{-1} of the

sample resulting in the overall throughput of 1.62×10^6 cells per min) due to a much higher sheath flow.[41] Even with lower applied powers and a high cell throughput, high separation efficiencies were still achieved.

This work focused on the development of a novel, SU-8-based SSAW device for high throughput enrichment of blood platelets at whole blood concentrations, although this approach is not limited to blood applications. The high separation efficiency and purity achieved in this device could also improve separation performance in other applications (cell washing, bacteria separation, *etc.*). Moreover, no significant shear-induced stress from the SSAW field was applied to the cells, as indicated by the low platelet activation in the flow cytometer, and is therefore harmless to the viability of blood cells as well as to comparable cell types. Conclusively, our technological approach and the realized device are versatile and can be taken from lab-based applications to real-world applications for future point-of-care diagnostics and therapeutics or for integration onto Lab-on-a-Chip platforms (Fig. 3).

Methods

Device fabrication

The SAW chips were fabricated based on a 4″ piezoelectric wafer of 128° YX black lithium niobate ($LiNbO_3$) (500 μm thick, double-side polished), according to procedures (I) to (VII) as outlined in Fig. 4(a). Shortly, (I) 1 μm of photoresist AZ 5214E was spin-coated onto the wafer for the patterning of the IDTs and electrodes (mask-less tabletop aligner, MLA100, Heidelberg Instruments), followed by a soft bake (90 °C, 3 minutes), exposure to UV light (365 nm, 22 mJ cm^{-2}), a reversal bake (120 °C, 3 minutes), flood exposure for 30 s (365 nm) and finally the development of the pattern using AZ 726 MIF developer (Microchemicals GmbH); (II) 295 nm of Al was deposited on 5 nm of Ti at 4 Å s^{-1} and 1 Å s^{-1}, respectively, *via* electron beam evaporation (Creamet 350 CL6, CreaVac GmbH), followed by a standard lift-off procedure; (III) rf-sputter deposition of 100 nm of stoichiometric silicone dioxide (SiOript2) (Creamet 350 CL6) was completed; (IV) the contact pads were etched *via* resist lithography and ion-beam etching (Mill150, Scia Systems GmbH); (V) a second lift-off photoresist mask was patterned for a Ti adhesion layer below the channel (parameters same as previous patterning step); (VI) 30 nm of Ti was deposited followed by a lift-off procedure; (VII) 50 μm of SU-8 50 was spin-coated onto the wafer for structuring of the SU-8 channel walls *via* rapid-prototyping optical laser lithography, followed by a soft bake (10 minutes at 65 °C, 30 minutes at 95 °C, cool down to 20 °C over 60 minutes), exposure to UV light (365 nm, 700 mJ cm^{-2}), a post exposure bake (1 minute at 65 °C, 10 minutes at 95 °C, cool down to 20 °C over 60 minutes) and finally the development of the structures using mr DEV 600 developer (Micro Resist Technology GmbH). The individual IDTs were designed as $\lambda/4$ and to be 50 Ω matched, with a 75 μm width and pitch, 20 finger pairs and an aperture of 3 mm. The fabricated SU-8 structures and IDTs can be seen in Fig. 4(b).

Once all the structures were completed, the wafer was mounted to a dicing foil and spin-coated with a protective resist layer for dicing of individual chips (150 μm wide blade, DAD3220, Disco Corp., Japan), followed by chip cleaning. For sealing of the SU-8 microchannels, a 5 mm thick rectangular PDMS block with cut-outs above the IDT locations and punched inlet-/outlet-openings, was created using a CNC milled aluminum mold and a standard PDMS mixture (Sylgard 184, Dow Corning Corporation) at a ratio of 10 : 1 by weight.

Device characterization

Characterization of the electrical behavior of the IDT pairs and the optimal driving frequencies, as used in the experiments, were obtained by *S*-parameter measurements using an electrical network analyzer (E5070B ENA Series, Agilent Technologies Inc). The driving frequencies obtained were 13.0 MHz for the focusing stage and 12.7 MHz for the separating stage with corresponding S11 values of 0.37 and 0.57, respectively (see Fig. S6†). In addition, a high frequency laser-Doppler vibrometry (Polytec UHF 120, Polytec GmbH) was used, as previously mentioned, to measure the standing wave field on the surface of the chip.

Simulations

To investigate the underlying physical phenomena that results in the focusing and separation of cells within the system, a 3D time-domain FEM simulation of a fully coupled SAW, excited by a sinusoidal electrical signal propagating on a $LiNbO_3$ wafer was modeled using COMSOL Multiphysics v5.4 on a custom workstation with 48 logical processors at 3 GHz operation frequency and 1 TB RAM (55 hours per simulation). The interaction of the wave field with a microfluidic channel bound by SU-8, or PDMS, walls and a PDMS cover, as well as the longitudinal wave field in the fluid domain were modelled. To accommodate for the specific crystal orientation of the $LiNbO_3$ substrate, the coordinate axis of the used tensor dataset for *z*-normal oriented $LiNbO_3$ was rotated 38° around the *x*-axis.[42] To

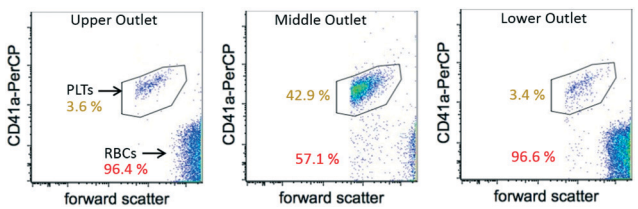

Fig. 3 Flow cytometer analysis for the collected blood cells. Flow cytometry scattergrams for the upper, middle, and lower outlet channels, showing the percentage of measured PLTs (circled) and RBCs. The logarithmic *x*-axis is the forward scatter and the logarithmic *y*-axis is the measured activity of the antibody CD41-PerCP-Cy5.5 (BD Biosciences, USA) which was used to label and identify the PLTs.

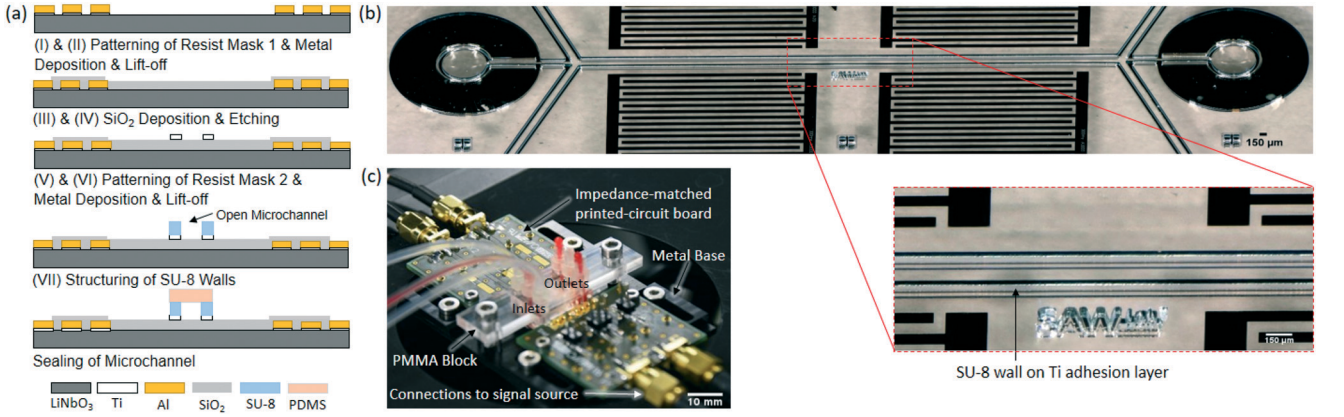

Fig. 4 Microfabrication procedure, and obtained structures of the SAW-based device. (a) Steps followed for the fabrication of the SU-8 microfluidic device, cross-sectional view. (I–II) Fabrication of the IDTs and contact pads, (III–IV) SiO_2 deposition and etching, (V–VI) fabrication of the Ti adhesion layer, (VII) structuring of the SU-8 channels walls. Following wafer dicing, a PDMS cover was used to seal the SU-8 channels. (b) Tilted optical microscope images of the fabricated SU-8 channels with underlying Ti. Insets show a close-up of certain structures. (c) Photograph of the device assembled in the custom chip-holder. RBCs and PLTs are pumped through the central inlet through silicone tubing and the RBCs can be seen exiting the side outlets.

generate SAW propagation on the substrate surface, a harmonic voltage was applied to rectangular equipotential surfaces that mimic the pattern of three pairs of IDT fingers per IDT (*i.e.* using a coupled electrostatic module), at the operational frequencies determined *via* network analysis and used for the sorting experiments. The thin metal loading was not considered in this study due to the high electrical conductivity and the low mass density of Al. In addition, the dielectric SiO_2 layer was neglected, as its thickness is much lower than the SAW wavelength. The amplitude of the applied voltages (68.5 V and 34.5 V for the focusing and separation stages, respectively) was adjusted to allow for the generation of substrate vertical displacement, whose magnitudes are identical to those generated experimentally and determined *via* a two-dimensional laser-Doppler wave field measurement. The coupling of waves into the fluid domain was modeled using the pressure acoustics set of equations (*i.e.* coupled pressure acoustic module) in the SU-8 and PDMS side walls ($\lambda/6$ wide), the PDMS cover (2λ thick), and the fluid domain ($\lambda/2$ wide) to acquire the acoustic pressure field distributions within the fluid-filled channel. The geometry was chosen based on different aspects. For the experiment, the side wall thickness ($\lambda/6$ = 50 µm wide) was selected based on previous investigations on channel wall adhesion: too thin walls (<25 µm) were easily delaminated, while too thick walls ($>\lambda_{SAW}/2$) led to strong SAW attenuation and lower energy efficiency. The channel width was adjusted to be half of the SSAW wavelength based on existing knowledge on SSAW particle sorting. The thickness of the PDMS was reduced to 2λ = 600 µm (from 4 mm in the experiment), to decrease computational expense, while ensuring at the same time, that BAW reflections will not reach the fluid in the given time-domain simulation time.

The bottom surface of the SU-8 side walls, and the fluid domain, were coupled to $LiNbO_3$ (500 µm thick) allowing for (i) transmission of the waves into the a fluid and (ii) effects arising from transmission and amplitude decay of the SAW through the walls to the fluid. To accurately capture the physics, a distributed mapped mesh with a highly fine mesh (minimum mesh size (h value) is 1.5×10^{-5} µm) near the interfaces, was used. The complete mesh comprises 215 400 domain elements, 52 420 boundary elements and 3640 edge elements. The number of degrees of freedom solved for was 4 937 853.

The key to the cell separator device represented here, is the difference in the force fields experienced by cells of different types and dimensions. To demonstrate the proposed concept, a simplified semi 3D frequency-domain FEM simulation was developed. Continuity boundary conditions were imposed on the front and back sides of the fluidic volume (x–z plane), mimicking the continuous channel used experimentally. Furthermore, matched impedance boundary conditions were used to avoid multiple reflections at the interfaces. Having imposed the conditions required to generate a representative time-averaged standing pressure field, the resultant radiation force induced on compressible PS particles (of similar size to the cells) was calculated using:[43,44]

$$F_{\mathrm{rad}} = \frac{1}{2}\rho_{\mathrm{f}}\int_{S_0}\left[\langle v_1^2\rangle - \frac{1}{\rho_{\mathrm{f}}^2 c_{\mathrm{f}}^2}\langle P_1^2\rangle\right]n\mathrm{d}S - \rho_{\mathrm{f}}\int_{S_0}\langle(n\cdot v_1)v_1\rangle\mathrm{d}S \quad (1)$$

where $\langle P_1^2\rangle$ and $\langle v_1^2\rangle$ are the mean square fluctuation of the pressure and velocity, respectively. ρ_{f} and C_{f} represent the density and sound speed of the fluid, respectively. The fluid is assumed to be in-viscid. All relevant parameters used in the simulations are given in Table S1.†

Experimental setup

Fabricated chips were placed in a custom chip holder and were electrically connected to a PowerSAW generator (BelektroniG GmbH) by gold-coated spring-pins and SMA

cables, in an impedance-matched printed-circuit board (Fig. 4(c)). RF signal splitters (SYPS-2-52HP+, Mini-Circuits) were used at both outlets of the PowerSAW generator to equally deliver power to each IDT in a pair. A highly viscous photoresist was manually applied between the IDTs and the contact pads in order to attenuate waves reflected from the chip edge. The PDMS cover, with pierced through-holes, was positioned on the chip surface with the inlets and outlets aligned, and a block of poly(methyl methacrylate) (PMMA) was fixed on top of the PDMS cover to apply pressure for proper contacting of the SU-8 channel walls. Permanent bonding of PDMS to SU-8 is possible, but was not favored here, as a removable cover permits easy cleaning between lab experiments and re-use of the device. The fluidic interconnections to low pressure syringe pumps (neMESYS 290N, Cetoni GmbH) were established to the PMMA *via* mini male luer connectors (Microfluidic Chip-Shop GmbH) and silicone tubing (ϕ: 1.02 mm, outer ϕ: 2.16 mm). Two 5 ml microsyringes (Borosilicate 3.3 glass syringe, ILS Innovative Laborsysteme GmbH) were used to house the sheath flow fluid and one 2.5 ml microsyringe was used for the sample solution. Experiments were conducted on the stage of an inverted light microscope (DMi5000 M, Leica Microsystems) and videos were recorded using a high speed camera (1000 fps with 200 μs exposure time, Phantom VEO 410, Vision Research Inc.).

Blood sample preparation and analysis

Human erythrocyte (RBC) and thrombocyte (PLT) concentrates were prepared and provided by the German Red Cross (DRK, Blutspendedienst Nord-Ost gGmbH, Dresden, Germany), and diluted samples were subsequently prepared in a solution of PBS with 2 mM of EDTA. For operation at whole blood concentration, the RBCs had a concentration of 5.1×10^9 cells per ml whereas the PLTs had a concentration of 3.0×10^8 cells per ml. Following the acoustofluidic separation experiments, the samples were collected at the different outlets and a flow cytometer (BD FACS Canto™ II, BD Biosciences) was used to analyze the results at the DRK facilities. 7.5×10^5 cells were stained with PerCP labeled antibody against CD41a and PE conjugated antibody against CD62P (both from BD) for 15 minutes. The reaction was stopped with cold cell wash (BD). A PE conjugated IgG1 antibody was used as an isotype control. For measurement of thrombocyte activation prior to staining, the cells were stimulated with 100 μM TRAP-6 for 15 minutes. All experiments with blood samples and the flow cytometry measurements were completed within 24 h of obtaining the samples.

Author contributions

Conceptualization: A. F., M. M.-S., T. T., A. W.; data curation: C. R., A. F., M. C., R. K.-W., A. W.; formal analysis: C. R., A. F., M. C., A. W.; funding acquisition: T. G., A. W.; investigation: C. R., A. F., M. C., F. S., R. K.-W., A. W.; methodology: C. R., A. F., F. S., R. K.-W., A. W.; project administration: T. T., M. M.-S., A. W.; resources: T. T., O. G. S., T. G.; software: A. F., A. W.; supervision: T. T., M. M.-S., O. G. S., T. G., A. W.; validation: T. T., A. W.; visualization: C. R., A. F., R. K.-W., A. W.; writing original draft C. R., A. F., A. W.; writing, review editing: C. R., A. F., R. K.-W., M. M.-S., O. G. S., A. W.

Conflicts of interest

There are no conflicts to declare.

Acknowledgements

This work was carried out within the EFRE InfraPro project "ChAMP: Chip-based acoustofluidic Medtech Platform" and also supported by German Research Foundation DFG (Gottfried Wilhelm Leibniz Price 2018 and FOR 1713 SMINT). The authors would like to thank all involved members of the IFW cleanroom, the SAWLab Saxony and the IFW workshop for production of the chip and the chipholder. We also wish to thank Dr. Dirk Groenewegen (Cells4Therapy BV) for the great support of our research and for his engagement enabling this study.

Notes and references

1 K. T. Kotz, W. Xiao, C. Miller-Graziano, W.-J. Qian, A. Russom, E. A. Warner, L. L. Moldawer, A. De, P. E. Bankey, B. O. Petritis, D. G. Camp, A. E. Rosenbach, J. Goverman, S. P. Fagan, B. H. Brownstein, D. Irimia, W. Xu, J. Wilhelmy, M. N. Mindrinos, R. D. Smith, R. W. Davis, R. G. Tompkins, M. Toner and I. the and P. the Host Response to Injury Collaborative Research, *Nat. Med.*, 2010, **16**, 1042–1047.
2 D. R. Gossett, W. M. Weaver, A. J. Mach, S. C. Hur, H. T. K. Tse, W. Lee, H. Amini and D. Di Carlo, *Anal. Bioanal. Chem.*, 2010, **397**, 3249–3267.
3 A. Lenshof and T. Laurell, *Chem. Soc. Rev.*, 2010, **39**, 1203–1217.
4 P. Neužil, S. Giselbrecht, K. Länge, T. J. Huang and A. Manz, *Nat. Rev. Drug Discovery*, 2012, **11**, 620.
5 M. Don, *JALA*, 2003, **8**, 72–81.
6 M. K. Litao and D. Kamat, *Pediatr. Ann.*, 2014, **43**, 417–420.
7 L. Gervais, N. de Rooij and E. Delamarche, *Adv. Mater.*, 2011, **23**, H151–H176.
8 A. M. Castro, A. O. Luquetti, A. Rassi, G. G. Rassi, E. Chiari and L. M. Galvao, *Parasitol. Res.*, 2002, **88**, 894–900.
9 C. E. Parker, T. W. Pearson, N. L. Anderson and C. H. Borchers, *Analyst*, 2010, **135**, 1830–1838.
10 Y. Song, Y.-Y. Huang, X. Liu, X. Zhang, M. Ferrari and L. Qin, *Trends Biotechnol.*, 2014, **32**, 132–139.
11 M. Wiklund, *Lab Chip*, 2012, **12**, 5283.
12 S. C. S. Lin, X. L. Mao and T. J. Huang, *Lab Chip*, 2012, **12**, 2766–2770.
13 G. Destgeer and H. J. Sung, *Lab Chip*, 2015, **15**, 2722–2738.
14 D. B. Go, M. Z. Atashbar, Z. Ramshani and H. C. Chang, *Anal. Methods*, 2017, **9**, 4112–4134.
15 M. Wu, Y. Ouyang, Z. Wang, R. Zhang, P.-H. Huang, C. Chen, H. Li, P. Li, D. Quinn, M. Dao, S. Suresh, Y. Sadovsky

and T. J. Huang, *Proc. Natl. Acad. Sci. U. S. A.*, 2017, **114**, 10584–10589.
16 J. J. Shi, X. L. Mao, D. Ahmed, A. Colletti and T. J. Huang, *Lab Chip*, 2008, **8**, 221–223.
17 M. E. Piyasena, P. P. A. Suthanthiraraj, R. W. Applegate, A. M. Goumas, T. A. Woods, G. P. Lopez and S. W. Graves, *Anal. Chem.*, 2012, **84**, 1831–1839.
18 X. Y. Ding, S. C. S. Lin, B. Kiraly, H. J. Yue, S. X. Li, I. K. Chiang, J. J. Shi, S. J. Benkovic and T. J. Huang, *Proc. Natl. Acad. Sci. U. S. A.*, 2012, **109**, 11105–11109.
19 D. J. Collins, B. Morahan, J. Garcia-Bustos, C. Doerig, M. Plebanski and A. Neild, *Nat. Commun.*, 2015, **6**, 8686.
20 A. Ozcelik, J. Rufo, F. Guo, Y. Gu, P. Li, J. Lata and T. J. Huang, *Nat. Methods*, 2018, **15**, 1021–1028.
21 X. Ding, Z. Peng, S.-C. S. Lin, M. Geri, S. Li, P. Li, Y. Chen, M. Dao, S. Suresh and T. J. Huang, *Proc. Natl. Acad. Sci. U. S. A.*, 2014, **111**, 12992–12997.
22 P. Li, Z. M. Mao, Z. L. Peng, L. L. Zhou, Y. C. Chen, P. H. Huang, C. I. Truica, J. J. Drabick, W. S. El-Deiry, M. Dao, S. Suresh and T. J. Huang, *Proc. Natl. Acad. Sci. U. S. A.*, 2015, **112**, 4970–4975.
23 Y. Gu, C. Chen, Z. Wang, P.-H. Huang, H. Fu, L. Wang, M. Wu, Y. Chen, T. Gao and J. Gong, *et al.*, *Lab Chip*, 2019, **19**, 394–402.
24 Microchem.com, SU-8 Photoresists, 2019, Available at: http://www.microchem.com/Prod-SU8.htm, [Accessed: 05.16.2019].
25 I. E. Obuh, V. Doychinov, D. P. Steenson, P. Akkaraekthalin, I. D. Robertson and N. Somjit, *IEEE Trans. Compon., Packag., Manuf. Technol.*, 2018, **8**, 1702–1710.
26 A. Lenshof, M. Evander, T. Laurell and J. Nilsson, *Lab Chip*, 2012, **12**, 684–695.
27 H. Bruus, *Lab Chip*, 2012, **12**, 20–28.
28 C. Witte, J. Reboud, R. Wilson, J. M. Cooper and S. L. Neale, *Lab Chip*, 2014, **14**, 4277–4283.
29 T. Saiki and Y. Utsumi, *Electron Commun Jpn*, 2014, **97**, 54–61.
30 C. Mu, Z. Zhang, M. Lin, Z. Dai and X. Cao, *Sens. Actuators, B*, 2015, **215**, 77–85.
31 A. Winkler, S. Harazim, S. Menzel and H. Schmidt, *Lab Chip*, 2015, **15**, 3793–3799.
32 A. Winkler, S. Harazim, D. Collins, R. Brünig, H. Schmidt and S. Menzel, *Biomed. Microdevices*, 2017, **19**, 9.
33 T. Laurell, F. Petersson and A. Nilsson, *Chem. Soc. Rev.*, 2007, **36**, 492–506.
34 M. Gedge and M. Hill, *Lab Chip*, 2012, **12**, 2998–3007.
35 H. Bruus, *Lab Chip*, 2012, **12**, 1014–1021.
36 P. Ohlsson, M. Evander, K. Petersson, L. Mellhammar, A. Lehmusvuori, U. Karhunen, M. Soikkeli, T. Seppä, E. Tuunainen, A. Spangar, P. von Lode, K. Rantakokko-Jalava, G. Otto, S. Scheding, T. Soukka, S. Wittfooth and T. Laurell, *Anal. Chem.*, 2016, **88**, 9403–9411.
37 F. Petersson, A. Nilsson, C. Holm, H. Jönsson and T. Laurell, *Lab Chip*, 2005, **5**, 20–22.
38 K. W. Cushing, F. Garofalo, C. Magnusson, L. Ekblad, H. Bruus and T. Laurell, *Anal. Chem.*, 2017, **89**, 8917–8923.
39 K. Yosioka and Y. Kawasima, *Acustica*, 1955, **5**, 167–173.
40 M. C. Jo and R. Guldiken, A Label-Free Cell Separation using Surface Acoustic Waves, *Proceedings of the 2011 Annual International Conference of the IEEE Engineering in Medicine and Biology Society*, Boston, MA, USA, 2011, pp. 7691–7694.
41 J. Nam, H. Lim, D. Kim and S. Shin, *Lab Chip*, 2011, **11**, 3361–3364.
42 G. Kovacs, M. Anhorn, H. E. Engan, G. Visintini and C. C. W. Ruppel, *IEEE Int. Ultrason. Symp.*, 1990, **1**, 435–438.
43 J. Dual, P. Hahn, I. Leibacher, D. Moller, T. Schwarz and J. T. Wang, *Lab Chip*, 2012, **12**, 4010–4021.
44 C. Devendran, N. R. Gunasekara, D. J. Collins and A. Neild, *RSC Adv.*, 2016, **6**, 5856–5864.